

A gravitational microlensing determination of continuum source size in Q2237+0305

J. S. B. Wyithe,¹ R. L. Webster,¹ E. L. Turner,² D. J. Mortlock¹

¹ *School of Physics, The University of Melbourne, Parkville, Vic, 3052, Australia*

² *Princeton University Observatory, Peyton Hall, Princeton, NJ 08544, USA*

Email: swyithe@physics.unimelb.edu.au, rwebster@physics.unimelb.edu.au, elt@astro.princeton.edu, dmortloc@physics.unimelb.edu.au

Accepted Received

ABSTRACT

Following the detection of a gravitational microlensing high magnification event (HME) in Q2237+0305A (Irwin et al. 1989; Corrigan et al. 1991) attempts have been made to place limits on the dimensions of the quasar continuum source. The analyses have studied either the observed event magnitude or the event duration. The latter approach has been hampered by a lack of knowledge about the transverse velocity of the lensing galaxy. We obtain both upper and lower statistical limits on the size of the continuum source from the observed HME using determinations of transverse velocity (Wyithe, Webster & Turner 1999b,c) obtained from the published monitoring data. Our calculations take account of the caustic orientation as well as the component of the caustic velocity that results from stellar proper motions. We find that the upper and lower limits on the magnified region of the continuum source are 6×10^{15} and 2×10^{13} cm respectively (99% confidence). Through consideration of the joint probability for source size and mean microlens mass we find that the mean mass lies between $\sim 0.01M_{\odot}$ and $\sim 1M_{\odot}$ (95% confidence).

Key words: gravitational lensing - microlensing - quasars.

1 INTRODUCTION

The object Q2237+0305 comprises a source quasar at a redshift of $z = 1.695$ that is gravitationally lensed by a foreground galaxy with $z = 0.0395$ producing 4 resolvable images with separations of $\sim 1''$. Each of the 4 images are observed through the galactic bulge, which has an optical depth in stars that is of order unity (eg. Kent & Falco 1988; Schneider et al. 1988; Schmidt, Webster & Lewis 1998). In addition, the proximity of the lensing galaxy means that the effective transverse velocity may be high. The combination of these considerations make Q2237+0305 the ideal object from which to study microlensing. Indeed, Q2237+0305 is the only object in which cosmological microlensing has been confirmed (Irwin et al. 1989; Corrigan et al. 1991).

The first confirmed high magnification event (HME) in image A had a measured rise time of ~ 26 days, followed by a subsequent event that had a decline of ~ 3 months. The resulting light-curve has been interpreted as a double peaked event corresponding to the source having crossed two fold caustics inside a cusp (Witt & Mao 1994), implying that the peak was caused by a single caustic crossing. The observation thus provides an estimate of the event crossing time, and a lower limit to the event amplitude. Attempts have subsequently been made on both of these fronts to

interpret the HME in terms of the size of the magnified continuum region (eg. Wambsganss, Paczynski & Schneider (1990); Rauch & Blandford 1991; Jaroszynski, Wambsganss & Paczynski 1992; Webster et al. 1991).

The amplitude of a HME is a function of source size - smaller sources produce events of larger amplitude. However, the event amplitude is also dependent on the width or strength of a caustic, a quantity that is the constant of proportionality in the near caustic approximation of Chang & Refsdal (1979). Witt (1990) termed this constant the flux factor and found that its value is distributed about a mean in the complex caustic structures that are produced by microlensing models. In addition this mean is a function of the average stellar mass in the model. Thus the event amplitudes have a distribution about an average that is model dependent. Wambsganss, Paczynski & Schneider (1990) produced a microlensing model with a mean microlens mass of $0.225M_{\odot}$ and found that the observed luminosity variation can be reproduced when the source has a radius smaller than $\sim 2 \times 10^{15}$ cm. Several attempts have been made to discuss the observed HME magnitude in terms of model continuum regions (eg. Rauch & Blandford 1991; Jaroszynski, Wambsganss & Paczynski 1992). These calculations suggest that current models of the continuum region can explain the observed HME amplitude. In addition, Lewis et al. (1998)

arXiv:astro-ph/9904361v1 26 Apr 1999

Table 1. Values of the total optical depth and the magnitude of the shear at the position of each of the 4 images of Q2237+0305. The quoted values are those of Schmidt, Webster & Lewis (1998). κ_* and κ_c are the optical depths in stars and in smoothly distributed matter respectively.

Image	$\kappa = \kappa_* + \kappa_c$	$ \gamma $
A	0.36	0.4
B	0.36	0.4
C	0.69	0.71
D	0.59	0.61

employ the observed difference in spectra obtained at two different epochs in combination with disc models to infer a continuum region that is $\lesssim 10^{15}$ cm.

A different approach is to use the observed event duration in combination with the transverse velocity to obtain an estimate of the source size. Approximate values have been obtained previously with the assumptions of a galactic transverse velocity of $v_t \sim 600 \text{ km sec}^{-1}$ (providing the caustic velocity with respect to the source), and a perpendicular caustic crossing (eg. Irwin et al 1989; Webster et al. 1991). These analyses have yielded values for the continuum source size that are consistent with those obtained through consideration of the event amplitude.

In this work we present an analysis of the source size that is required to produce the observed event duration from model light-curves. This work follows results for the limit on the galactic transverse velocity that we have obtained previously (Wyithe, Webster & Turner 1999b,c). In this analysis we consider the effect of a stellar velocity dispersion as well as the angle of caustics with respect to the source trajectory on the caustic crossing time.

2 THE MICROLENSING MODEL

2.1 Microlensing models for Q2237+0305

Throughout the paper, standard notation for gravitational lensing is used. The Einstein radius of a $1M_\odot$ star in the source plane is denoted by η_0 . The normalised shear is denoted by γ , and the convergence or optical depth by κ . The model for gravitational microlensing consists of a very large sheet of point masses that simulates the section of galaxy along the image line-of-sight, together with a shear term that includes the perturbing effect of the mass distribution of the lensing galaxy as a whole. The normalised lens equation for a field of point masses with an applied shear in terms of these quantities is

$$\vec{y} = \begin{pmatrix} 1 - \kappa_c - \gamma & 0 \\ 0 & 1 - \kappa_c + \gamma \end{pmatrix} \vec{x} + \sum_{j=0}^{N_*} m_j^j \frac{(\vec{x}^j - \vec{x})}{|\vec{x}^j - \vec{x}|^2} \quad (1)$$

Here \vec{x} and \vec{y} are the normalised image and source positions respectively, and the \vec{x}_i are the normalised positions of the point masses. κ_c is the optical depth in smoothly distributed matter. To construct a microlensed light-curve Eqn 1 is solved for the macroimage magnification at many points along a predefined source trajectory through the inversion technique of Lewis et al. (1993) and Witt (1993).

For the microlensing models of Q2237+0305 presented in the current work we assume the macro-parameters for the lensing galaxy calculated by Schmidt, Webster & Lewis (1998). These values are shown in table 1. Two models are considered for the distribution of microlenses, one with no continuously distributed matter, and one where smooth matter contributes 50% of the surface mass density. Both the microlensing rate due to a transverse velocity (eg. Witt, Kaiser & Refsdal 1993), as well as the corresponding rate due to proper motions (Wyithe, Webster & Turner 1999a) are not functions of the details of the microlens mass distribution, but rather are only dependent on the mean microlens mass. We therefore limit our attention to models in which all the point masses have the same mass since the results obtained will be applicable to other models with different forms for the mass function.

Each of our models was computed for a source track of length $10\eta_0$. We set the minimum number of stars to be used in our models at 500. Two orientations were chosen for the transverse velocity with respect to the galaxy, with the source trajectory being parallel to the A–B and C–D axes. At each orientation, 100 simulations were made for each of the 4 images of Q2237+0305 in combination with each of the model mass distributions. The two orientations bracket the range of possibilities, and because the images are positioned approximately orthogonally with respect to the galactic centre correspond to shear values of $\gamma_A, \gamma_B < 0, \gamma_C, \gamma_D > 0$ and $\gamma_A, \gamma_B < 0, \gamma_C, \gamma_D > 0$ respectively.

For our analysis we assume that microlensing is produced through the combination of a galactic transverse velocity with an isotropic velocity dispersion. Moreover, we assume that the magnitude of the dispersion is the same at the position of each of the four images. For the line-of-sight velocity dispersion of the stars in the galactic bulge we take the theoretical value of $\sigma_* \sim 165 \text{ km sec}^{-1}$. The microlensing models presented in this work have been discussed in detail in Wyithe, Webster & Turner (1999c).

2.2 The effective transverse velocity and the effect of random proper motions

We define the effective transverse velocity as the transverse velocity that produces a microlensing rate from a static model equal to that of the observed light-curve. The effective transverse velocity therefore describes the microlensing rate due to the combination of the effects of a galactic transverse velocity and proper motion of microlenses.

To obtain limits on the effective transverse velocity, many simulations are made which have a sampling rate and period that are identical to the published monitoring data (Irwin et al. 1989, Corrigan et al. 1991, Østensen et al. 1996). Observational errors are also simulated. The simulations used for the current work treated the quoted random component (± 0.02 magnitudes in Irwin et al. 1989) of the observational uncertainty in two ways. Firstly as a $\pm 2\sigma$ error in images A and B, and a $\pm 1\sigma$ error in images C and D, and secondly as a $\pm 1\sigma$ error in images A and B, and a $\pm \frac{1}{2}\sigma$ error in images C and D. The simulations employed in the determination of the effective transverse velocity assume a point source. For the current work 5000 sampled simulations were produced at each transverse velocity from the 100 $10\eta_0$ simulations for each model. The procedure for

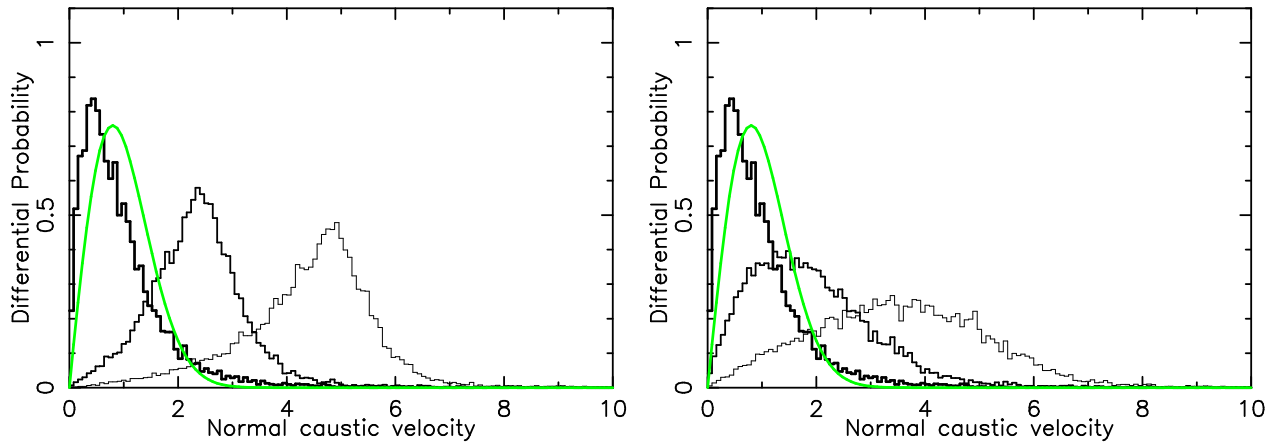


Figure 2. The probability distribution functions of normal caustic velocities. The thin, medium and thick lines correspond to transverse velocities of $v_t = 0, 2.5$ and $5\times$ the average projected speed of the stellar velocity dispersion respectively. The thin light line shows the distribution of stellar speeds. Left: The applied shear is positive ($\gamma > 0$). Right: The applied shear is negative ($\gamma < 0$).

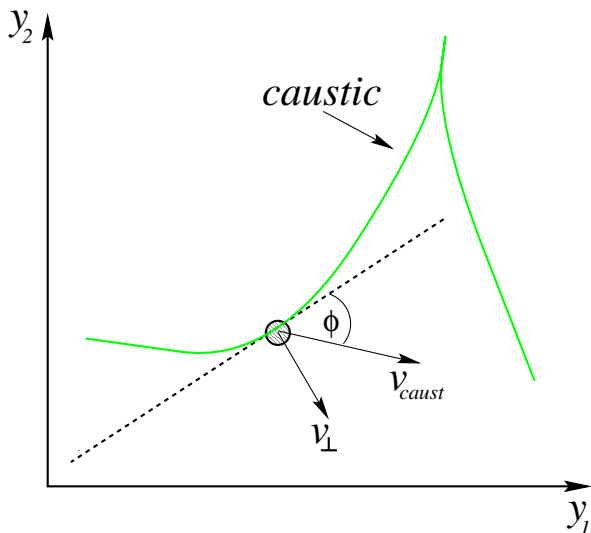


Figure 1. A schematic of the geometry of a caustic crossing a source.

computing the cumulative probability ($P_v(v_{tran} < V | \langle m \rangle)$) that the effective galactic transverse velocity is less than an assumed value (for a given microlens mass $\langle m \rangle$) is described in Wyithe, Webster & Turner (1998c). The function $P_v(v_{tran} < V | \langle m \rangle)$ was computed under two assumptions for the Bayesian prior and was found to be quantitatively consistent in those cases. The priors assumed that $p_v(v_{tran}) \propto dv_{tran}$ and $p_v(v_{tran}) \propto \frac{dv_{tran}}{v_{tran}}$ respectively.

The galactic transverse velocity is obtained from the effective transverse velocity by comparing the microlensing rates in terms of the histogram of light curve derivatives. The procedure is outlined in Wyithe, Webster & Turner (1999b).

There is a simple scaling that relates models of the same optical depth but consisting of model stars with a different mass. The dimensionless Einstein radius of a point mass is \sqrt{m} . If all masses in the model are reduced by a factor a , then all physical distances (in both the source and lens

planes) between dimensionless coordinates are reduced by a factor \sqrt{a} . The gradient of the light-curve therefore scales as $1/\sqrt{a}$, and the measurement of effective transverse velocity that is made within the context of a given model through comparison with a data set is proportional to \sqrt{a} . However the distribution of caustic velocities that is produced from random proper motion is insensitive to the mean microlens mass. This scaling allows a microlensing model to be applicable to models with many different mean masses.

3 SOURCE SIZE

The HME in image A observed during late 1988 is described by 5 observations (Irwin et al. 1989; Corrigan et al. 1991) that constrain a peak in the light-curve. We assume that the length of the HME of is twice the estimated rise time of 26 days (Corrigan et al. 1991). To measure the size of the source continuum region we consider the observed event length of 52 days in light of the calculations of transverse velocity that we have made previously (Wyithe, Webster & Turner 1999b). We use these values of transverse velocity in combination with calculations of the normal caustic velocities that arise from the proper motion of stars, as well as the orientations of tangents to the caustic points.

The velocity of the caustic network resulting from the stream motion of a starfield was calculated by Schramm et al. (1993). This result was generalised by Kundic, Witt & Chang (1993) so that the velocity of individual caustic points due to the proper motion of stars could be determined. We use the expressions obtained to find the velocities of caustic points in the y_1 and y_2 directions. The vector addition of these components is in general in a direction other than that which is normal to the caustic at that point. Therefore we also calculate the caustic gradient. The method of calculating both the caustic location and gradient are described below.

We implement the contouring algorithm as described by Lewis et al. (1993). The image curves are followed in discrete steps in one direction. During the contouring algorithm the

occurrence of the image line crossing a critical curve results in the image magnification changing sign due to a parity flip between the critical images on either side of the critical curve. The location of the critical curve can then be found through a search for the image position that produces a lens mapping (Eqn 1) Jacobian determinant of zero. This value for the critical image position is used in the expressions for caustic velocity. The gradient of the caustic tangent is found by first computing the location of a point a short distance along the critical curve in both directions. The corresponding caustic points are then used to compute the gradient of the caustic tangent from a three-point derivative.

In each of the models considered we found the distribution of caustic velocities and gradients by searching for caustics along an equal length of source track in two orthogonal directions. The source tracks were each $10\eta_o$ in length and were computed from a separate model starfield. We computed the properties of the caustics that intersect with 500 such source tracks in both the directions that are parallel ($\gamma > 0$) and perpendicular ($\gamma < 0$) to the shear. This is equivalent to finding the caustic locations on a 500×500 line grid covering a $10\eta_o \times 10\eta_o$ square of source plane, although the use of 1000 starfields makes the sample more statistically representative.

Figure 1 is a schematic representation of the determination of the normal caustic velocity from the caustic velocity and gradient. The caustic velocity is the vector addition of the transverse velocity (v_{tran1}, v_{tran2}) and the contribution to caustic velocity that results from stellar proper motion (v_1, v_2). The normal caustic velocity \vec{v}_\perp is computed from the components of the caustic velocity ($\vec{v}_{caust} = (v_1 + v_{tran1}, v_2 + v_{tran2})$) in combination with the relative orientation between the tangent to the caustic and the caustic velocity vector. The magnitude of the normal caustic velocity is:

$$v_\perp = |\vec{v}_\perp| = |\vec{v}_{caust} \times \sin(\phi)|, \quad (2)$$

where ϕ is the angle between the tangent to the caustic and the caustic velocity. A caustic that has a velocity which makes a small angle with the tangent to the caustic sweeps out a smaller area per unit length per unit velocity than one which has a velocity normal to its tangent. Therefore, to calculate the distribution of normal caustic velocities at a stationary source position, each value of v_\perp carries a weight of $|\sin(\phi)|$.

Figure 2 shows probability distributions of normal caustic velocities. All velocities on this plot are in units of the projected mean speed of the stellar velocity dispersion. The left and right hand diagrams correspond to the cases of positive and negative galactic shear respectively. Distributions are shown in each case for the normal caustic velocities due to the stellar proper motions alone (thick line), and in combination with a transverse velocity in the y_1 direction of 2.5 (medium line) and 5.0 (thin line). Also plotted in figure 2 is the distribution of stellar speeds (light line). These diagrams demonstrate the dependence of the mean normal caustic velocity on the direction of a transverse velocity. Note however that the result is independent of the sign of the shear in the case where there is no transverse velocity. When the transverse velocity is lined up with the direction of the caustic clustering ($\gamma < 0$) the resulting normal caustic velocity is lower on average than when the

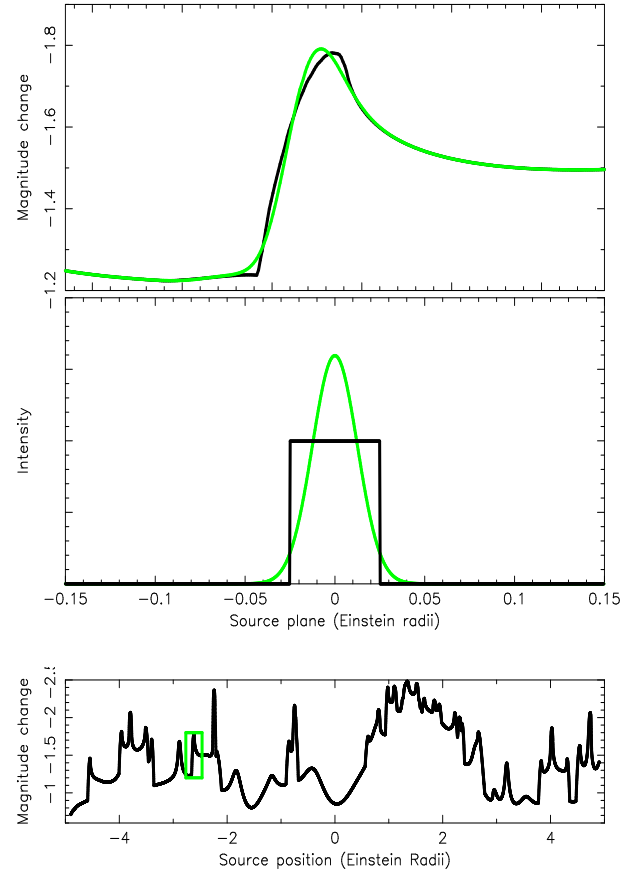


Figure 3. Bottom: A sample light-curve for image A ($\gamma_A = +0.4$) of Q2237+0305. One half of a double peaked event is highlighted by a box and reproduced in the top panel. Centre: A top-hat intensity profile (dark line), and a Gaussian intensity profile (light line). Top: A plot of the highlighted HME showing the details of the event shapes that result from the two source intensity profiles.

transverse velocity is perpendicular to it ($\gamma > 0$). This is because the tangent to the caustic is more likely to lie along the source trajectory.

For a small source ($S_s \ll \eta_o$) the crossing time of the caustic is $\Delta T = S_s/v_\perp$, where S_s is the source diameter. Therefore, the dimension of the source in a direction normal to the caustic is

$$S_s = v_\perp \times \Delta T. \quad (3)$$

This expression demonstrates that there is a systematic uncertainty in our determination of source size that is proportional to the uncertainty in the estimate of the event length.

In this paper we assume that the projected source profile is circular so that the event time is not dependent on the source orientation. Eqn 3 defines our measure of source size. The interpretation of this size however is dependent on the profile of the source. The lower panel in figure 3 shows an example of an extended source light-curve for Image A ($\gamma_A = +0.4$) computed using the method described in Wyithe & Webster (1999). One half of a double peaked event in this light-curve is highlighted by a box. This event is reproduced in the top panel of figure 3 for two source in-

tensity profiles, a Gaussian profile (light line) and a top-hat profile (dark line). Cross-sections of these intensity profiles are shown in the central panel of figure 3 with a scale equal to that which produced the HME. This figure demonstrates that if the source profile was described by a top-hat function then S_s is approximately the source diameter. However, if the profile is Gaussian then the measured radius will be approximately twice its half width.

Limits on the source size are obtained from Eqn 3 by considering the distribution of the normal caustic velocity in combination with the observed event length. To obtain the distribution of source size, $p_s(S_s | \langle m \rangle)$ we integrate the probability distributions for caustic velocity at a given transverse velocity, $p_c(v_\perp | \langle m \rangle, v_{tran})$ over the probability distribution of transverse velocity, $p_v(v_{tran} | \langle m \rangle)$. $p_v(v_{tran} | \langle m \rangle)$ is obtained from the derivative of the cumulative distribution, $P_v(v_{tran} < V | \langle m \rangle)$ following the correction for the contribution of stellar proper motion to the value of effective transverse velocity (Wyithe, Webster & Turner 1999b). The expression for $p_s(S_s | \langle m \rangle)$ is

$$p_s(S_s | \langle m \rangle) = \frac{1}{\Delta t} \int p_c(v_\perp | \langle m \rangle, v_{tran}) p_v(v_{tran} | \langle m \rangle) dv_{tran}. \quad (4)$$

3.1 Determination of source size

The results of our source size estimates are presented in Figures 4 and 5, and Table 2. Values are given that correspond to assumed mean microlens masses of $0.1M_\odot$ and $1.0M_\odot$. Figures 4 and 5 show cumulative and differential distributions of source size $P_s(S_s < R | 0.1M_\odot)$ (thin lines), $P_s(S_s < R | 1.0M_\odot)$ (thick lines), and $p_s(S_s | 0.1M_\odot)$ (thin lines), $p_s(S_s | 1.0M_\odot)$ (thick lines). The solid and dotted lines correspond to simulated errors of $\pm 2\sigma$ in images A, B, $\pm 2\sigma$ in images C, D, and of $\pm 1\sigma$ in images A, B, $\pm \frac{1}{2}\sigma$ in images C, D respectively. Table 2 shows the upper and lower 99%, 95%, and 90% limits as well as the mean of the distributions $p_s(S_s | 0.1M_\odot)$ and $p_s(S_s | 1.0M_\odot)$. The values are given for the two directions assumed for the transverse velocity as well as for simulations that contain 0% and 50% smoothly distributed matter. Two columns are shown for each limit with values corresponding to an assumed error that is $\pm 2\sigma$ in images A, B, $\pm 1\sigma$ in images C, D, and $\pm 1\sigma$ in images A, B, $\pm \frac{1}{2}\sigma$ in images C, D respectively. We find that the source size lies between the values of $2 \times 10^{13} cm$ and $6 \times 10^{15} cm$ (98% level).

The values obtained demonstrate that while the measured lower limit of source size is not very sensitive to the mass assumed for the model, the upper limit is larger when a higher mean microlens mass is assumed. This trend is demonstrated in figures 4 and 5, and can be understood as follows. The limit of effective transverse velocity measured is proportional to $\sqrt{\langle m \rangle}$ and therefore has a value that is more likely to be low or zero for lower assumed values of mean microlens mass. The lower limits of source size come from the lowest velocity caustics, and these are produced by the stellar proper motions alone, hence the insensitivity to the microlens mass. However the upper limits are produced from the fastest moving caustics. These are a result of the combination of the stellar proper motions with the upper limits to transverse velocity. The upper limits are mass dependent

and hence so to are the upper limits to source size. This effect is magnified in the smooth matter case. The transverse velocity that is measured by a model that contains smoothly distributed matter is larger than that measured by one containing only point masses. This is due to the more sparsely distributed caustic network and the more linear nature of the fold caustics (Wyithe, Webster & Turner 1999c). The upper limit of source size that is measured is therefore more dependent on the mass assumed if the model smooth matter content is higher.

As mentioned, there is an increased probability for high velocity caustics in the case where the assumed mass is higher. The mean of the source size distribution therefore increases with mass. However because the most likely transverse velocity is low, the lower end of the distribution is independent of the mass assumed. The resulting source size distribution is therefore highly asymmetric. In addition the mode is between $\sim 1 \times 10^{14} cm$ and $4 \times 10^{14} cm$ for all models considered.

It is apparent from figures 4 and 5 that the size of the photometric error assumed is an important factor in the determination of the limits on source size. The effect of the size of the error is however more significant where the assumed mean mass is higher. This is because the error effects the measurement of transverse velocity, a factor that contributes to the high velocity caustics and hence to the large source size measurements. Once again the resulting variation in transverse velocity measurement does not significantly effect the determination of the lower limits as these are produced by caustic velocities that result from stellar proper motion. The effect is more significant upon the introduction of smooth matter into the models since there is then a larger discrepancy between the measured effective transverse velocity and the equivalent transverse velocity.

Both the lower and upper limits of source size are insensitive to the direction assumed for the transverse velocity when the assumed microlens mass is $0.1M_\odot$. This is because the most likely transverse velocity is zero so that the caustic velocities are produced by stellar proper motions. However if the mass is assumed to be $1.0M_\odot$ then while the lower limit remains insensitive, the upper limits vary due to the variation in the measurement of transverse velocity.

The co-dependence of mean microlens mass and source size is now treated more rigorously.

3.2 Simultaneous limits of mean microlens mass and source size

In Sec. 3.1 the normalised probability distributions, $p_s(S_s | \langle m \rangle)$, that the continuum source size is between S_s and $S_s + dS_s$ given that the mean microlens mass is $\langle m \rangle$, were obtained. The probability that the source size lies in the above range and the mean microlens mass is between $\langle m \rangle$ and $\langle m \rangle + d\langle m \rangle$ is then given by

$$p_{m,s}(S_s, \langle m \rangle) = p_s(S_s | \langle m \rangle) p_m(\langle m \rangle), \quad (5)$$

where $p_m(\langle m \rangle)$ is the probability that the mean microlens mass is between $\langle m \rangle$ and $\langle m \rangle + d\langle m \rangle$. p_m is a known function, given in Wyithe, Webster & Turner (1999c), that is approximately independent of the source size. $p_m(\langle m \rangle)$ was determined under the same assumptions of the Bayesian prior for the galactic transverse velocity as the function $p_v(v_{tran})$.

Table 2. Table showing the upper and lower 99%, 95%, and 90% limits as well as the mean of the distributions $p_s(S_s | 0.1M_\odot)$ and $p_s(S_s | 1.0M_\odot)$. The values are given for the two directions assumed for the transverse velocity as well as for simulations that contain 0% and 50% smoothly distributed matter. Two columns are shown for each limit with values corresponding to an assumed error that is $\pm 2\sigma$ in images A, B, $\pm 1\sigma$ in images C, D, and $\pm 1\sigma$ in images A, B, $\pm \frac{1}{2}\sigma$ in images C, D respectively.

0% Smooth Matter															
Mean Mass	Trajectory Direction	$S_{low}(99\%)$ ($\times 10^{14} cm$)	$S_{low}(95\%)$ ($\times 10^{14} cm$)	$S_{low}(90\%)$ ($\times 10^{14} cm$)	Mean ($\times 10^{14} cm$)	$S_{up}(90\%)$ ($\times 10^{14} cm$)	$S_{up}(95\%)$ ($\times 10^{14} cm$)	$S_{up}(99\%)$ ($\times 10^{14} cm$)							
$0.1M_\odot$	$\gamma_A, \gamma_B > 0$	0.244	0.238	0.637	0.617	1.01	0.972	6.70	6.52	12.1	11.9	16.6	16.2	29.2	29.0
$1.0M_\odot$	$\gamma_A, \gamma_B > 0$	0.394	0.280	1.10	0.746	1.80	1.19	12.7	8.48	24.1	16.0	31.3	21.7	49.2	36.6
$0.1M_\odot$	$\gamma_C, \gamma_D > 0$	0.240	0.237	0.622	0.614	0.982	0.968	6.56	6.50	11.9	11.9	16.3	16.2	29.1	29.0
$1.0M_\odot$	$\gamma_C, \gamma_D > 0$	0.370	0.272	1.03	0.723	1.67	1.16	11.9	8.11	22.6	15.2	29.2	20.5	46.0	35.1

50% Smooth Matter															
Mean Mass	Trajectory Direction	$S_{low}(99\%)$ ($\times 10^{14} cm$)	$S_{low}(95\%)$ ($\times 10^{14} cm$)	$S_{low}(90\%)$ ($\times 10^{14} cm$)	Mean ($\times 10^{14} cm$)	$S_{up}(90\%)$ ($\times 10^{14} cm$)	$S_{up}(95\%)$ ($\times 10^{14} cm$)	$S_{up}(99\%)$ ($\times 10^{14} cm$)							
$0.1M_\odot$	$\gamma_A, \gamma_B > 0$	0.207	0.187	0.556	0.493	0.895	0.795	5.95	5.31	11.1	9.75	14.6	13.3	24.0	23.2
$1.0M_\odot$	$\gamma_A, \gamma_B > 0$	0.487	0.274	1.45	0.772	2.48	1.26	16.4	10.1	30.1	19.4	38.1	25.7	58.4	40.4
$0.1M_\odot$	$\gamma_C, \gamma_D > 0$	0.206	0.188	0.553	0.495	0.888	0.796	5.73	5.27	10.5	9.57	13.1	13.2	23.3	23.0
$1.0M_\odot$	$\gamma_C, \gamma_D > 0$	0.468	0.272	1.36	0.760	2.26	1.23	14.5	9.25	26.8	17.7	33.7	23.2	49.3	36.7

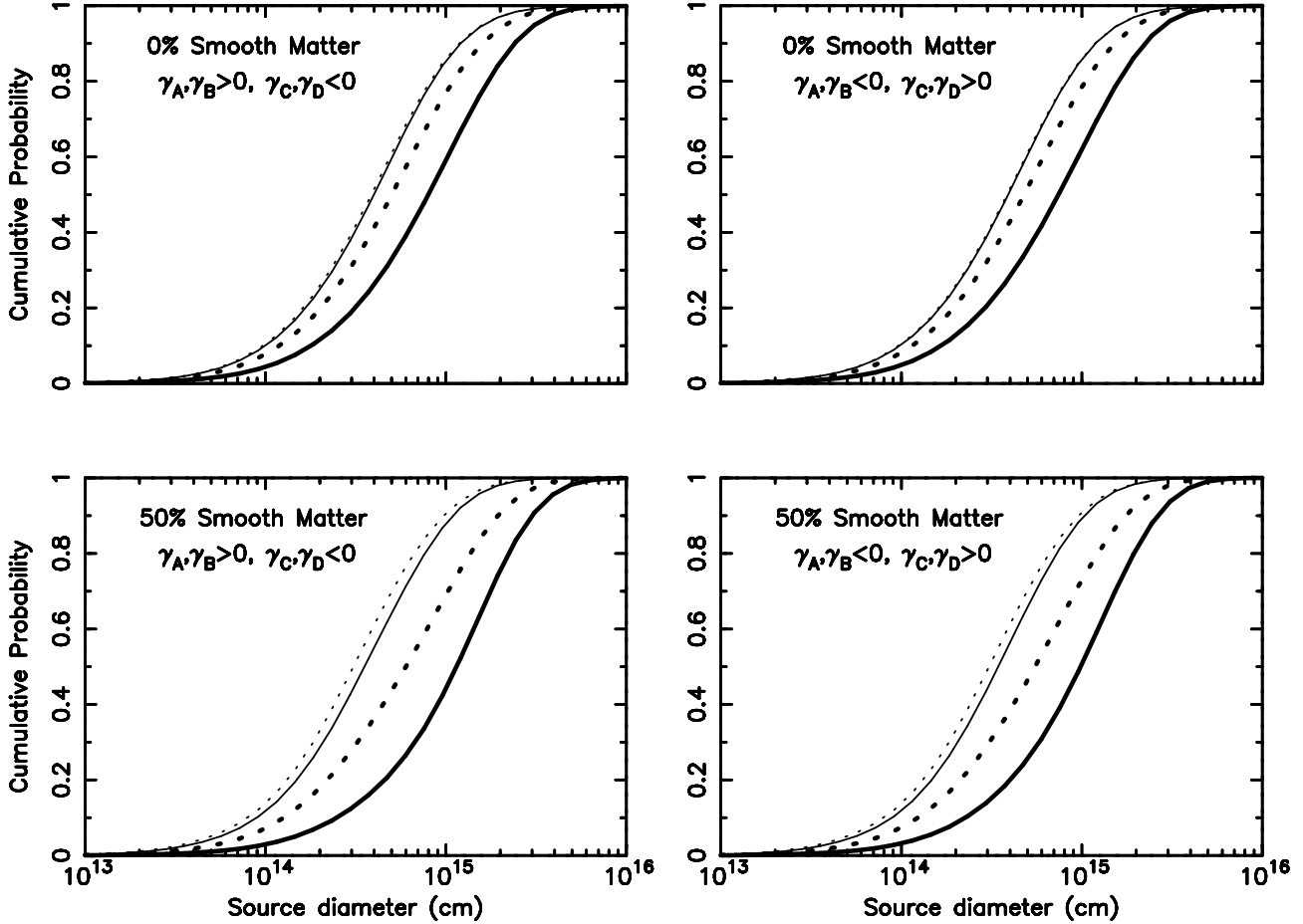


Figure 4. The cumulative distributions of source size $P_s(S_s < R | 0.1M_\odot)$ (thin lines) and $P_s(S_s < R | 1.0M_\odot)$ (thick lines). The solid and dotted lines correspond to simulated errors of $\pm 2\sigma$ in images A, B, $\pm 2\sigma$ in images C, D, and of $\pm 1\sigma$ in images A, B, $\pm \frac{1}{2}\sigma$ in images C, D respectively.

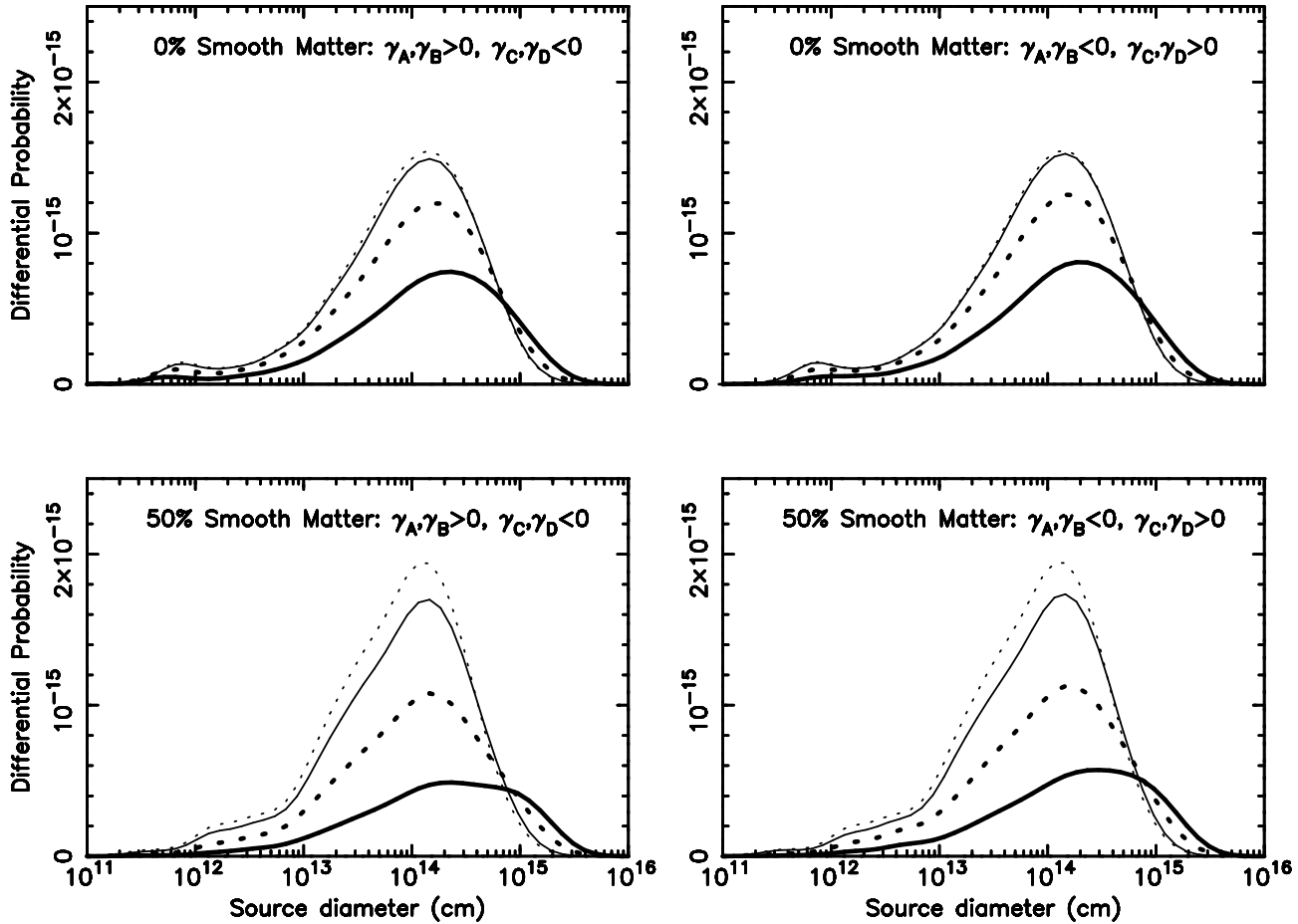


Figure 5. The differential distributions of source size $p_s(S_s | 0.1M_\odot)$ (thin lines) and $p_s(S_s | 1.0M_\odot)$ (thick lines). The solid and dotted lines correspond to simulated errors of $\pm 2\sigma$ in images A, B, $\pm 2\sigma$ in images C, D, and of $\pm 1\sigma$ in images A, B, $\pm \frac{1}{2}\sigma$ in images C, D respectively.

Figure 6 shows contour plots of the two-dimensional distribution $p_{m,s}$ for the assumed source orientations, smooth matter fraction and photometric errors. All possible combinations of the two values of each parameter are included, so that eight models are shown. The contours are at 3.6, 14, 26, 61 per cent of the peak height, and so the extrema of the relevant contours represent 4σ , 3σ , 2σ , and 1σ limits on the single variables. The most likely model is that $\langle m \rangle \simeq 0.05 - 0.2M_\odot$ (dependent on the content of smooth matter assumed) and $S_s \simeq 2 \times 10^{14}$ cm (independent of model).

The most important benefit of combining the distributions of S_s and $\langle m \rangle$ is that an upper limit can be placed on the mean microlens mass. The limits on $\langle m \rangle$ are subject to both random and systematic uncertainties, with the measured mass increasing with photometric errors and decreasing with the fraction of smooth matter. Assuming that the chosen values for these parameters bracket the likely models, upper and lower limits for $\langle m \rangle$ can be found by using the most extreme values of the contour limits. This yields the 95 per cent result that $0.01M_\odot \lesssim \langle m \rangle \lesssim 1M_\odot$. The upper limit is lower than that obtained by Lewis & Irwin (1996), although sufficiently high that it does not conflict

with any popular models of galactic halos or bulges. Similarly, the contour maxima yield the result that there is a 95 per cent chance that 5×10^{12} cm $\lesssim S_s \lesssim 10^{15}$ cm. At a given confidence level, both the upper and lower limits of source size, and the lower limit of mean microlens mass have smaller values in Figure 6 than those obtained in previous sections and Wyithe, Webster & Turner (1999c). This can be attributed to the asymmetric nature of the distribution in both dimensions.

4 CONCLUSION

The observed peak in the light-curve of image A of Q2237+0305 in 1988 appears to be one half of a double peaked event that is characteristic of a source having passed inside of a cusp. If this interpretation is correct then the observed peak is the result of the source having been crossed by a single caustic. The observations therefore provide a good record of the caustic crossing time. The source size is the product of the event length and the normal velocity of the caustic involved. We have placed limits on normal caustic velocities by combining measurements of the

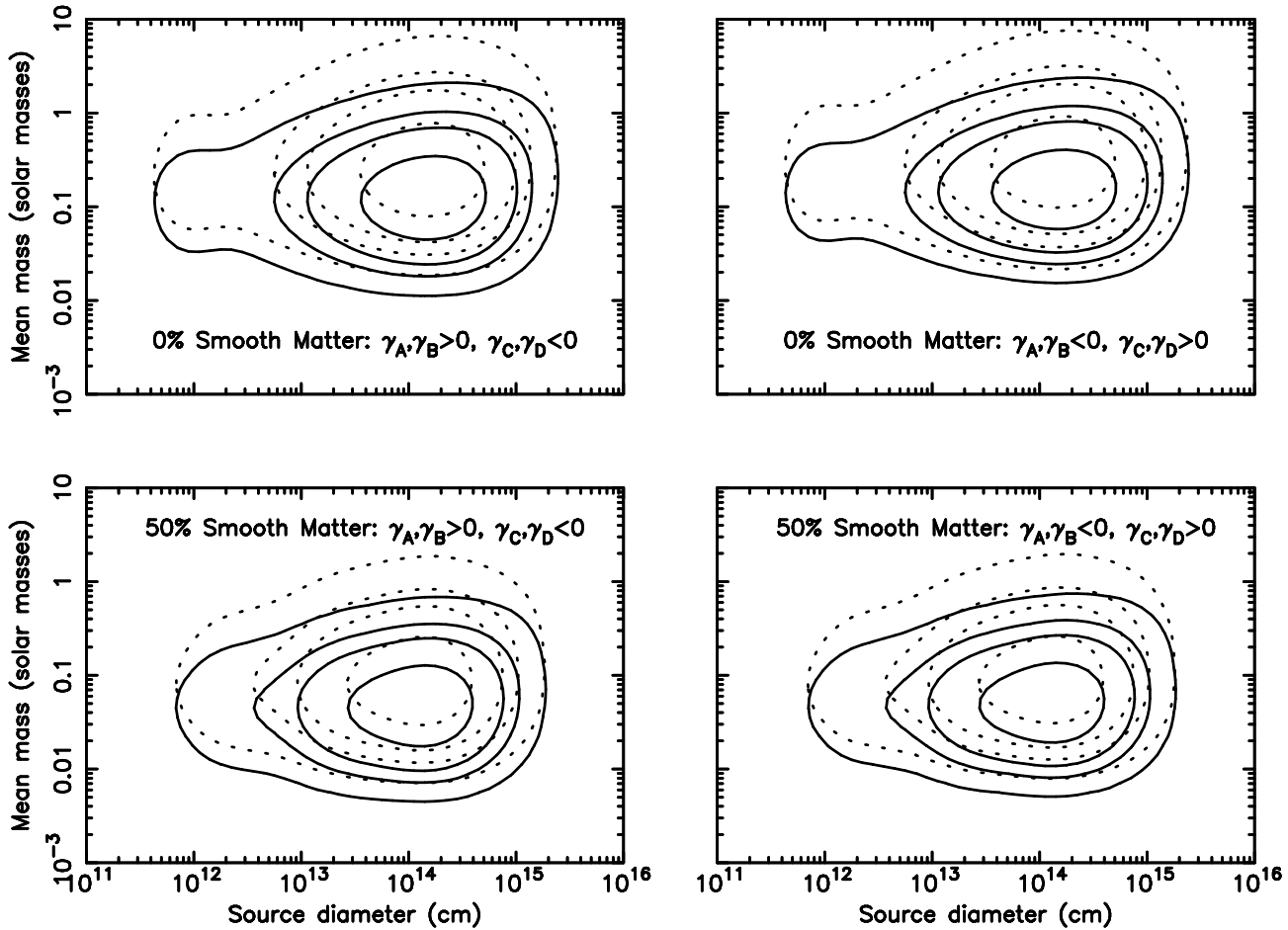


Figure 6. Contours of percentage peak height of the function $p(S_s, \langle m \rangle)$. The contours shown are the 3.6%, 14%, 26% and 61% levels. The solid and dotted lines correspond to simulated errors of $\pm 2\sigma$ in images A, B, $\pm 2\sigma$ in images C, D, and of $\pm 1\sigma$ in images A, B, $\pm \frac{1}{2}\sigma$ in images C, D respectively.

galactic transverse velocity based on the entire set of published monitoring data with calculations of the distributions of caustic gradients as well as the component of the caustic velocities that result from stellar proper motions. We find that the most likely size of the magnified continuum region is $S_s \sim 2 \times 10^{14} \text{ cm}$, and that the upper and lower limits are $S_s \sim 6 \times 10^{15} \text{ cm}$ and $S_s \sim 2 \times 10^{13} \text{ cm}$ (99% level) respectively. Simultaneous consideration of microlens mass and source size has provided an upper limit to the mean microlens mass of $1M_\odot$ that was unavailable from consideration of the microlensing rate alone.

It was noted in Wyithe, Webster & Turner (1999b) that the statistical determination of the effective transverse velocity will be aided when monitoring data from a longer period becomes available. The narrowing of the likelihood for the effective transverse velocity will in turn provide tighter limits on the mean microlens mass and source size. At a known transverse velocity, the component of uncertainty due to the range of event lengths that can be produced by a source will be reduced upon the observation of more HME durations. Thus the extent of the contours in figure 6 will be reduced as more monitoring data becomes available.

REFERENCES

- Chang, K., Refsdal, S., 1979, *Nature*, 282, 561
 Corrigan et.al, 1991, *Astron. J.*, 102, 34
 Foltz, C. B., Hewitt, P. C., Webster, R. L., Lewis, G. F., 1992, *Ap. J.*, 386, L4 3
 Irwin, M. J., Webster, R. L., Hewitt, P. C., Corrigan, R. T., Jędrzejewski, R. I., 1989, *Astron. J.*, 98, 1989
 Jaroszynski, M., Wambsganss, J., Paczynski, B., 1992, *Ap. J.*, 396, L65
 Kent, S. M., Falco, E. E., 1988, *Astron. J.*, 96, 1570
 Kundic, T., Witt, H. J., Chang, K., 1993, *Ap. J.*, 409, 537
 Lewis, G. F., Irwin, M. J., 1996, *MNRAS* 283, 225
 Lewis, G. F., Irwin, M. J., Hewitt, P. C., Foltz, C. B., 1998, *MNRAS*, accepted
 Lewis, G. F., Miralda-Escude, J., Richardson, D. C., Wambsganss, J., 1993, *MNRAS*, 261, 647
 Østensen, R. et al. 1996, *Astron. Astrophys.*, 309, 59
 Rauch, K. P., Blandford, R. D., 1991, *Ap. J.* 1991, 381, L39
 Schmidt, R. W., Webster, R. L., Lewis, G. F. 1998, *MNRAS*, 295, 488
 Schneider, D. P., Turner, E. L., Gunn, J. E., Hewitt, J. N., Schmidt, M., Lawrence, C. R., 1988, *Astron. J.*, 95, 1619
 Schramm, T., Kayser, R., Chang, K., Nieser, L., Refsdal, S., 1993, *Astron. Astrophys.*, 268, 350
 Wambsganss, J., Paczynski, B., Schneider, P., 1990, *Ap. J.*, 358,

L33

- Webster, R. L., Ferguson, A. M. N., Corrigan, R. T., Irwin, M. J., 1991, *Astron. J.*, 102, 1939
- Witt, H. J., 1990, *Astron. Astrophys.*, 236, 311
- Witt, H. J., 1993, *Ap. J.*, 403, 530
- Witt, H. J., Kayser, R., & Refsdal, S. 1993, *Astron. Astrophys.*, 268, 501
- Witt, H. J., Mao, S., 1994, *Ap. J.*, 429, 66
- Wyithe, J. S. B, Webster, R. L., 1999, *MNRAS* accepted
- Wyithe, J. S. B, Webster, R. L., Turner, E. L., 1999a, *MNRAS* submitted
- Wyithe, J. S. B, Webster, R. L., Turner, E. L., 1999b, *MNRAS* submitted
- Wyithe, J. S. B, Webster, R. L., Turner, E. L., 1999c, *MNRAS* submitted